Remote Sensing of Environment 239 (2020) 111621

Contents lists available at ScienceDirect

Remote Sensing of Environment

journal homepage: www.elsevier.com/locate/rse

Flight tests of the computational reconfigurable imaging spectrometer

C.M. Wynn*, J. Lessard, A.B. Milstein, P. Chapnik, Y. Rachlin, C. Smeaton, S. Leman, S. Kaushik, R.M. Sullenberger

Massachusetts Institute of Technology, Lincoln Laboratory, 244 Wood Street, Lexington, MA 02421, USA

ARTICLE INFO

Edited by: Jing M. Chen

Keywords:
Hyperspectral imaging
Airborne
Computational imaging
Uncooled microbolometer
Thermal infrared

ABSTRACT

We present the first flight data using a Computational Reconfigurable Imaging Spectrometer (CRISP) system. CRISP (Sullenberger et al., 2017) is a novel hyperspectral thermal imaging spectrometer that uses computational imaging to enable high sensitivity measurements (via spectral multiplexing) from smaller, noisier, and less-expensive components (e.g., uncooled microbolometers) making it useful on small space and air platforms with strict size, weight, and power requirements. In contrast to other multiplexing hyperspectral solutions (e.g Michelson interferometer), it does not require moving parts, allowing for a robust system without aggressive engineering solutions. We discuss flight system design and calibration. Spectra from ground targets and gaseous species are compared to performance expectations. We successfully demonstrate the ability to extract airborne longwave infrared (8–12 μm) imagery and spectra from an uncooled camera-based CRISP system.

1. Introduction

Hyperspectral imaging (HSI) spectrometers create images containing 10's to 1000's of spectral channels and are operational over much of the optical spectrum. Multispectral systems contain ~3–10 channels. This is in contrast to traditional color images, which contain only three visible channels of spectral information. Principally, each HSI pixel in an image contains a spectrum of the material being observed. As such, chemical or material identification of each pixel is possible, providing a unique data product useful in a wide range of science and technology applications, such as environmental monitoring, biomedical imaging, surveillance, food safety inspection and control, agricultural monitoring, and mineralogy (Manolakis et al., 2016).

The fundamental challenge of HSI is to collect what is in essence a 3D data cube using only a 2D focal plane array. This challenge has been met via a number of clever solutions (Hagen and Kudenov, 2013). Perhaps the most common of these is the pushbroom (Lucey et al., 1998) or slit spectrometer, wherein only a single strip of the scene is imaged at a given time, with the orthogonal axis of the focal plane used to collect the spectral information. Successive strips are collected to achieve a 2D image. A successful example of this is the well-known SEBASS system operating in the longwave infrared (LWIR, 8–12 μm) (Hackwell and et al., 1996).

Improvements in the optical throughput (with a commensurate reduction in acquisition time or improvement in area coverage rate) have been achieved using spectral multiplexing. Spectral multiplexing involves capturing all the spectral information on a single pixel, and subsequently decoding the spectrum via a variety of other means (all of which require additional measurements of the scene). The Michelson Fourier Transform Infrared (FTIR) solution is perhaps the most successful and common HSI system utilizing spectral multiplexing. Multiple measurements of the scene are made under different interference conditions via the use of a moving mirror, after which the spectrum is recovered using a Fourier transform operation. The mirror must be controlled with optical scale precision in order to successfully decode the spectra. Variants of the Michelson interferometer include the Sagnac interferometer, which has been successfully used for HSI (Lucey et al., 2008; Honniball et al., 2016). Because of the need for precise moving parts, FTIR systems are more likely to be used in satellites, e.g. the Cross-Track Infrared Sounder (CrIS) (Han et al., 2013), as opposed to aircraft because motion jitter is less severe (Manolakis et al., 2016). Very recently, an FTIR HSI system operating with a cooled detector in the LWIR was flown on an airplane (Agassi et al., 2016).

The Computational Reconfigurable Imaging Spectrometer (CRISP) system is a recently developed (Sullenberger et al., 2017) HSI system, which, like the FTIR systems, utilizes multiplexing to enable higher optical throughput. In contrast to FTIR systems, CRISP does not require moving parts, instead relying upon an encoding mask (at an intermediate image plane) and platform motion to collect successive looks at a ground sample area. Spectra are recovered from these successive looks via inversion of the data by utilizing the (known) encoding mask

* Corresponding author.
E-mail address: cwynn@ll.mit.edu (C.M. Wynn).

https://doi.org/10.1016/j.rse.2019.111621
Received 6 September 2019; Received in revised form 10 December 2019; Accepted 20 December 2019
Available online 06 January 2020

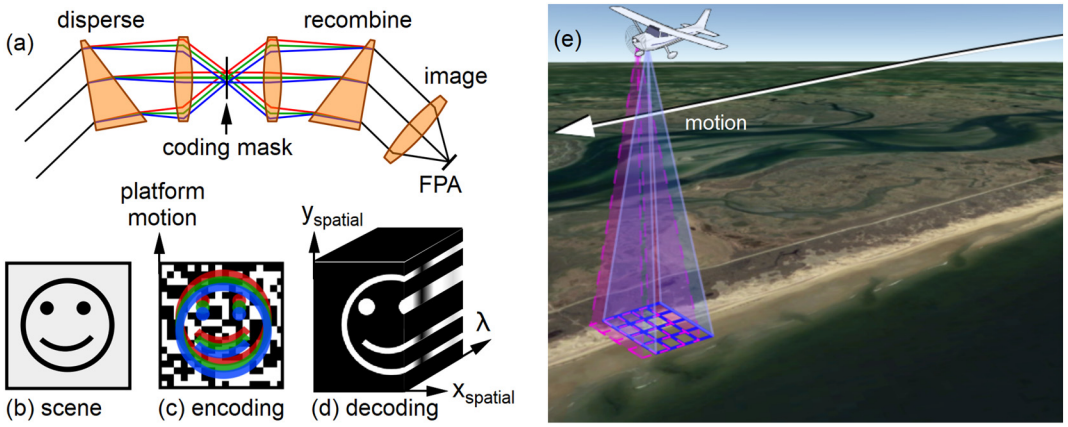

Fig. 1. CRISP measurement scheme. (a) Optical setup. The scene's (b) colors are dispersed by a prism and focused onto an encoding mask, as depicted in (c). The colors are then recombined using a second prism and imaged by a microbolometer camera. After sufficient unique measurements (which are obtained as the dispersed scene travels across the mask due to platform motion), the collected data can be inverted to yield the hyperspectral cube as shown in (d). Concept of operations for a CRISP system collecting data from an aircraft (e).

pattern. The CRISP approach for HSI enables two sensitivity gains, (1) the traditional Fellgett or multiplex advantage found in other multiplexed measurement designs and (2) an additional coding gain. As the along-track format size of the focal plane array grows beyond the minimum number of platform shifts needed to reconstruct the data cube, the measurement becomes more overdetermined, and the signal-to-noise (SNR) of the reconstructed data cube continues to improve. The result, which we refer to as coding gain, is that the SNR grows ever-larger in proportion to the square root of the along-track focal plane array format size (Sullenberger et al., 2017).

The coding and Fellget gains can be obtained simultaneously in practical designs and applications. These gains are especially pronounced for detector-noise limited focal planes such as uncooled microbolometer arrays.

CRISP utilizes a dual-disperser reimaging design (Fig. 1), with a static encoding mask in the image plane, and relies on platform motion to achieve coding diversity. In addition to the lack of moving parts, this design provides an additional advantage in that it reduces spectral distortion. Most HSI systems suffer from unavoidable spectral distortions known as “smile” and “keystone” (Mouroulis et al., 2000). These effects are inherent to spectral systems in which the light impinges on the dispersive element at different angles dependent on their position within the scene. The constructive interference condition is shifted by their relative angles and thus different colors will appear shifted dependent upon their height in the scene. FTIR systems do not have a dispersive element, but nonetheless suffer from changes in optical path difference dependent upon position within the focal plane. The typical solution to this issue is to spectrally calibrate each pixel separately. The dual dispersers in the CRISP design are expected to minimize these image-position-dependent effects since the second prism undoes the effect of the first (ideally recombining all spectral energy back into a given pixel), and thus minimizing these distortions.

An additional advantage of the CRISP architecture is that it collects a full 2D image of the scene with each captured frame, in contrast to the pushbroom imagers. This opens up the possibility of using CRISP raw image data to do frame-to-frame image registration applying computer vision techniques and thus reduce the effects of platform jitter and/or eliminate the need for an inertial navigation system (INS).

A remote LWIR HSI system provides numerous capabilities of great interest to the earth sensing community. These capabilities include the ability to remotely monitor trace LWIR-active gas plumes, such as methane (CH_4) and ammonia (NH_3), both of which have spectroscopic signatures in the LWIR (Leifer et al., 2017). Moreover, gases can be detected concurrently using standard spectral identification algorithms. CH_4 is a greenhouse gas with a global warming potential 100× that of carbon dioxide (CO_2) (Myhre et al., 2013), and NH_3 contributes significantly to the atmospheric nitrogen budget. The ability to monitor them with high spatial and temporal resolution is thus of great utility as it allows gas lifetimes and transport processes to be identified. Remote LWIR HSI systems can also be used to track properties of plants such as surface temperature and emissivity, which can be extracted via appropriate separation algorithms (Meerdink et al., 2019b). Note that plant temperature and emissivity are unavailable via visible-shortwave infrared spectroscopy. Plant temperature is important as it indicates a plant's response to the local environment and can be used as an indicator of plant stress (Calderón et al., 2013). Emissivity provides information relating to the outer layers of a leaf, in contrast to visible light, which penetrates to the more deep structures of the leaf. The ability to deploy a small form factor airborne LWIR HSI (such as on a drone) has significant potential value in precision agriculture due to the aforementioned ability to extract temperature and spectral information. Such utility was demonstrated by mounting a broadband thermal camera and spectrometer on a drone (Zarco-Tejada et al., 2012). The small form factor enabled by CRISP's sensitivity gains (vide infra) open up the possibility of improved temperature estimates via its ability to extract a full LWIR spectrum.

Historically, high spectral sensitivity from an LWIR HSI system required a low-noise cryogenically-cooled focal plane array (FPA). Cooling presents a size and power challenge in certain scenarios. In some applications, coolant lifetimes will limit operational lifetimes. CRISP presents a means of achieving high sensitivity from a smaller package by using a noisier uncooled FPA and regaining performance via its multiplex advantage. Multiplex gain scales with FPA size, and uncooled LWIR focal plane arrays continue to increase in pixel count. CRISP's small form factor thus has great potential for use in small form factor satellites, which are becoming increasingly common both in government and industry. It sets up the possibility of affordably putting an array of small satellites in place for a cost similar to a single larger satellite. Such a system offers the possibility of improved revisit and coverage rates compared to current capabilities. The small form factor could also be applicable to small-payload drone operations.

The CRISP design utilizes a fixed mask with no moving parts. This is advantageous operationally in that it is much less sensitive to vibrations than competing alternatives such as FTIR-based systems. As such, a CRISP-based system is well-suited for airborne-based measurements similar to the results reported in this paper.

2. Spectrometer system

2.1. System design/description

The CRISP concept was originally designed and tested using a breadboard system designed from commercial off-the-shelf (COTS) components. We chose a design in the LWIR using an uncooled microbolometer camera (significantly noisier than state-of-the-art HgCdTe detectors) because a detector-noise limited system best showcases the CRISP advantages. LWIR is also quite useful for the detection of gaseous plumes (Manolakis et al., 2019). This breadboard system uses a 50 Hz 640 × 480 resolution microbolometer camera with 17 μm pixels and 52 mm, f/1 lenses (aspheric triplets) by FLIR (model A655sc), ZnSe dispersive prisms (no antireflective coating), and an antireflective coated ZnSe encoding mask with a randomly-chosen binary grid applied using contact lithography. The feature sizes of the encoding mask are matched to the pixel size of the imager. The instantaneous field of view (IFOV) of each pixel is 410 μrad. Using this breadboard we successfully demonstrated the CRISP concept on a variety of targets in the laboratory, including blackbody radiators and trace gases (Sullenberger et al., 2017).

The flight system (Fig. 2) uses the same design as the laboratory breadboard, with several improvements. The optical throughput was significantly improved via two modifications: (1) the 30° ZnSe prisms were anti-reflection (AR) coated improving their optical transmission from 70% to 94%, and (2) the position of the final prism was moved closer to the final lens to reduce vignetting and increase field-of-view (FOV) and throughput. The flight system was mechanically ruggedized to withstand handling during transport and the vibrational environment inside of an aircraft. All adjustable optomechanical mounts were eliminated and replaced with custom designed fixed, rugged mounts. The prisms and encoding mask were held in their rigid mounts using custom-made RTV 566 gaskets, specifically designed to eliminate stresses due to thermal expansion/contraction. The CRISP optical components were mounted onto a rigid 25 mm thick aluminum plate for increased ruggedization. A GoPro visible camera (Hero6; 60 Hz; 2704 × 1520 pixels; 85.5° × 55.2° FOV) was added to provide reference imagery in the visible spectrum. The entire spectrometer assembly was enclosed in an aluminum environmental box with a thermostat-regulated heater unit designed to maintain a stable temperature (21°). The CRISP system sees outside of the environmental box through a 75 mm diameter AR coated germanium window, equipped with an RTV 566 gasket.

Georeferencing and timing information was recorded using an Applanix POS AV V510 V5 OEM with LN-200 IMU which provided INS/GPS information at a rate of 200 Hz. The system has a 140 μrad absolute precision in pitch/roll and a 1222 μrad absolute precision in heading. Relative drift is 8727 μrad/h. Each image captured by the CRISP system includes a GPS timestamp.

2.2. Ground characterization

The flight system was tested before installation on the airplane and showed generally similar performance as the laboratory breadboard. The optical throughput improved from 11% (breadboard) to 21% (flight system). These values are for an extended object, which is impacted by an occluded field of view due to the final prism location and size. Note that the encoding mask contributes a 50% throughput loss.

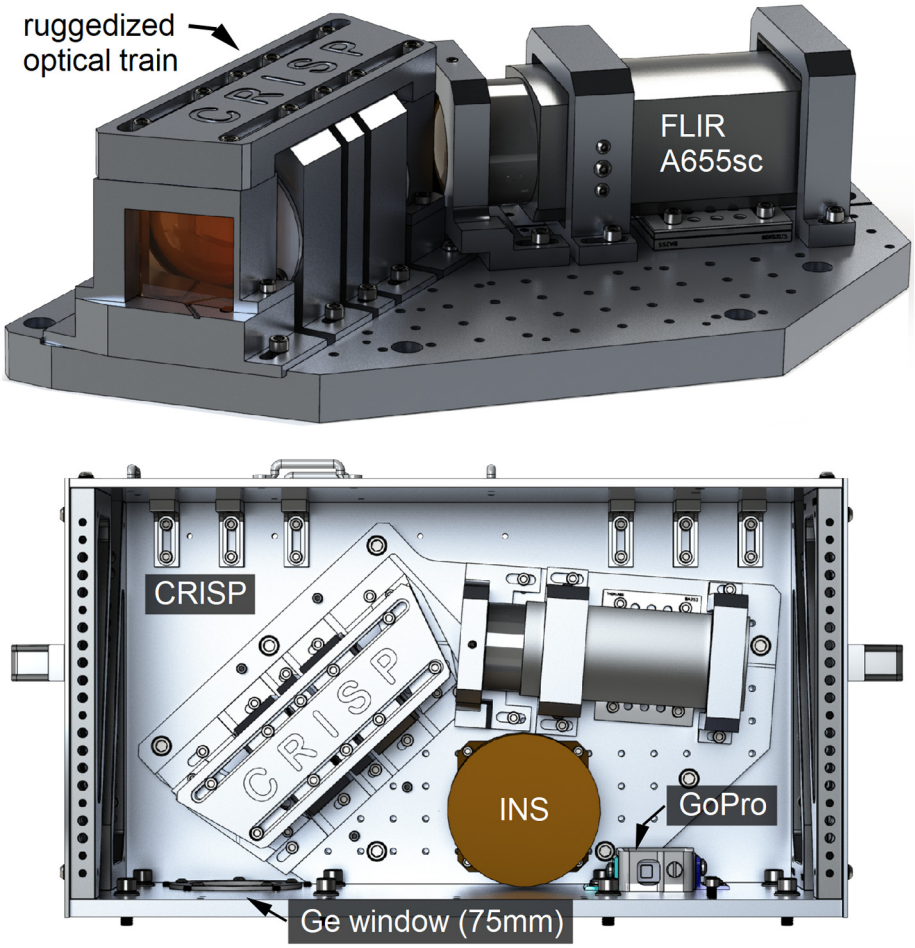

Fig. 2. CRISP flight instrument, ruggedized spectrometer components assembly (top), and spectrometer components integrated into environmental box (bottom).

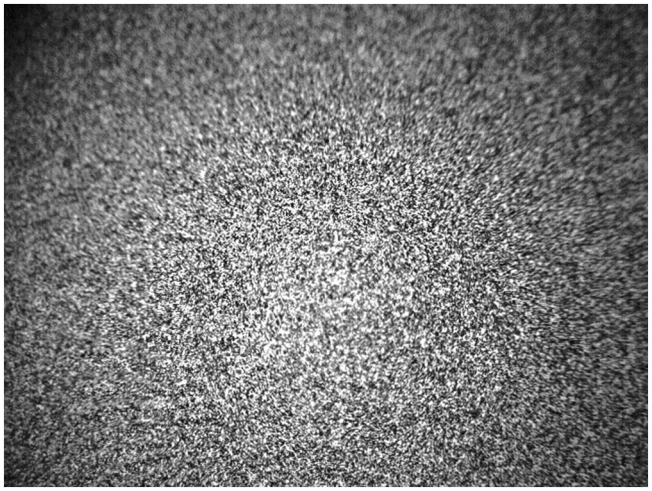

Fig. 3. CRISP system "mask function" measured using 8.85 μm flat field from the output port of an integrating sphere.

Critical to the successful demultiplexing of CRISP spectra is knowledge of the "mask function", which encodes the spectral rays. The mask itself is a 50 mm diameter ZnSe window with printed aluminum features (in a randomly-chosen binary grid) intended to block the transmission of light in certain positions. The mask features were designed to be 17 μm in size, matched 1:1 with the microbolometer pixel size. Due to diffraction and optical aberrations, the actual mask transmission ("mask function") is not binary but rather grayscale. This grayscale "mask function" is measured by peering into an integrating sphere illuminated by a rastered quantum cascade laser (QCL) with $\lambda = 8.85$ μm via the CRISP system. The "mask function" we measured is shown in Fig. 3. The measurement was completed by averaging 1000 frames collected peering into the integrating sphere with the laser on, and subtracting a background consisting of a 1000 frame average with the laser turned off. We note that the 17 μm pixels of our imager and the same sized features in our encoding mask are smaller than the diffraction-limited point spread function (PSF) in the LWIR (~20–34 μm). The optical design of the CRISP system yields $N_\lambda = 67$ spectral bins across 7.7–14 μm, a mean resolution of $\Delta\lambda = \sim 94$ nm.

Background radiation due to Narcissus (an image of the detector itself created by a reflection from the mask) as well as the room temperature optical mounts and elements were measured by peering into a pool of liquid nitrogen. This background image (an average of 1000 frames) was subtracted from the raw data prior to CRISP processing.

The flight system was designed to be robust enough that our ground calibration would be sufficient for flight data collection, i.e. no need for in-flight calibration. The "mask function" in addition to reference target spectra was measured both before and after the flight. The target spectra showed no change (within our spectral resolution), and the "mask function" showed very little change as well, indicating that our mechanical and thermal design was sufficient to achieve our stability goals.

A radiometric calibration was performed using a CI Systems NIST-traceable extended area blackbody radiator, which was varied from 20 °C to 125 °C while CRISP spectra were recorded [Fig. 4 (top)]. Assuming our source was Lambertian, these yielded sensitivities of 0.00039 $CRISP_{signal}$/μflick (8–9 μm) to 0.00018 $CRISP_{signal}$/μflick (11–12 μm), where 1 μflick = 10^{-6} W/sr/cm^2/μm. Given a noise floor of 0.0205 $CRISP_{signal}$, the noise equivalent spectral radiance (NESR) was calculated for several wavelength bands [Fig. 4 (bottom)].

The spectral response function (SRF) describes how each spectral channel responds to different wavelengths. The SRF of the CRISP system was measured using a tunable QCL directed into an integrating sphere and rastered slightly with a fast steering mirror to eliminate

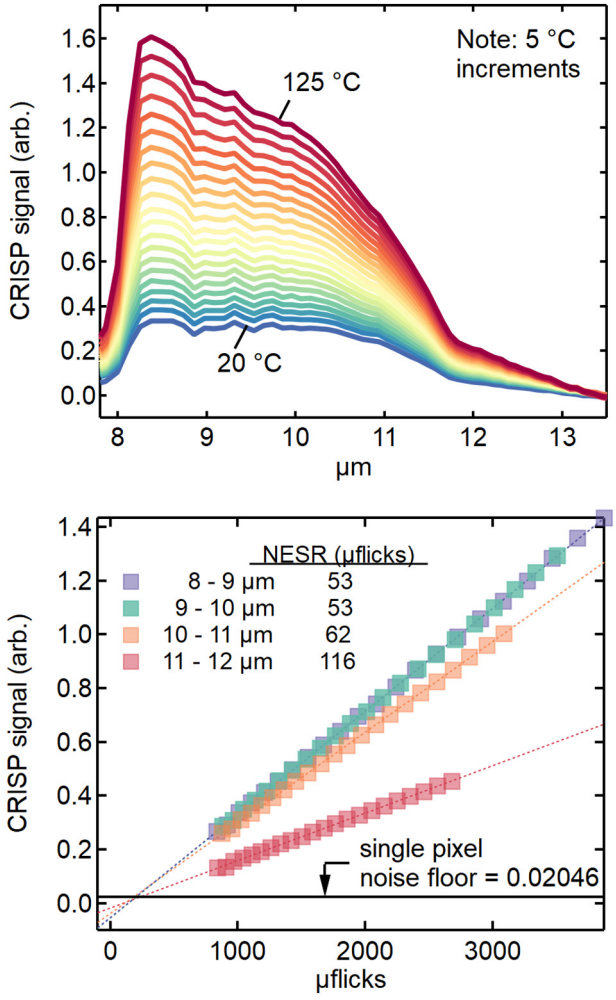

Fig. 4. Radiometric Calibration of the CRISP system. Response of the system to a blackbody at various temperatures (top): Signal as a function of spectra radiance, assuming a Lambertian blackbody emitter (bottom).

speckle effects. CRISP images of the narrowband flat field light emanating from the integrating sphere were collected and processed (see schematic in Fig. 5a) for $\lambda = 8.75$–9.4 μm with a step size of $\Delta\lambda = \sim 7.9$ nm. For our 30° prism design, dispersion yields a theoretical spectral bin width of 0.117 μm/px (17 μm pixels) around the vicinity of $\lambda = 8.9$ μm.

Given the design of the CRISP system, we expect the SRF to be directly related to the Airy disk created by the f/1 optics. Theoretical dispersion and Airy disk calculations are shown in Fig. 5b. The full width half maximum (FWHM) of the Airy disk for our f/1 optics and 8.9 μm light is calculated to be $FWHM_{Airy} = 18.2$ μm, or $FWHM_{Airy}$/px = 1.07. We measured a FWHM of the SRF to be $FWHM_{SRF} = 0.147$ μm (mode value from all pixels in the imager) by plotting the intensity in the $\lambda = 8.9$ μm bin versus QCL wavelength (see Fig. 5c). The $FWHM_{SRF}$ to bin width ratio yields a value of 1.25. This is a 15.5% difference compared to the theoretical value of 1.07, a discrepancy most likely due to lens imperfections and slight misalignments in the optical system. A heatmap and histogram for the pixels processed in the SRF measurement is shown in Fig. 5d (right). The axes indicate the location of the pixel during the start of the CRISP measurement (which included 423 frames of data total). We note that the bottom 2/3 of the focal plane has significantly better performance than the top 1/3. Using the same datasets, we were able to make a SNR heatmap, as shown in Fig. 5d (right). We calculate SNR as the peak height at the illumination wavelength to the standard deviation of the noise off

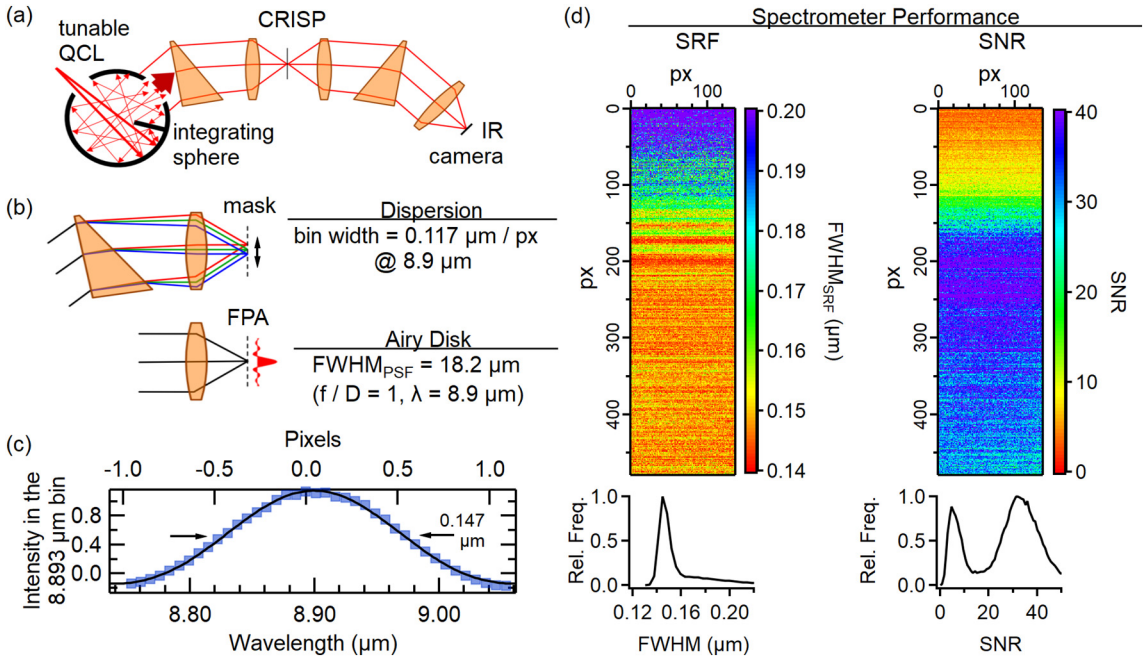

Fig. 5. Spectral response function (SRF) measurement of the CRISP system. (a) SRF measurement setup. A tunable quantum cascade laser (QCL) is injected into an integrating sphere to provide a narrow bandwidth flat field for the spectrometer. (b) The theoretical dispersion created by one of the CRISP prisms is 0.117 µm/px in the vicinity of 8.9 µm light. The Airy disk (calculated) for $\lambda = 8.9$ µm is 18.2 µm (FWHM) for an f/1 system. (c) SRF of the CRISP spectrometer (typical). The FWHM of the SRF curve is 0.147 µm. (d) SRF and SNR heatmaps. The x- and y-dimensions represent the starting pixel location for a measurement of 350 frames.

wavelength. Similar to the SRF heatmap, the SNR heatmap shows better performance on the bottom 2/3 of the focal plane compared to the top 1/3. These trends are due to the "mask function" having higher contrast in the bottom 2/3 compared to the top 1/3 (as clearly seen in Fig. 3). In fact, there is a direct linear correspondence between SNR and "mask function" contrast (row-by-row standard deviation of the measured mask function). This nonuniformity in image contrast (and resultant SNR) is a direct result of our use of non-optimal commercial lenses. An optimized optical design is currently being developed for our next generation sensor.

Spectral distortion was evaluated using a field of straight line targets each of width < 1 ground-sample distance (GSD). The dominant distortion in these CRISP images was small and consistent with aberrations from the final lens in the optical chain (closest to the camera). No evidence of smile or keystone aberrations was evident.

3. Flight test objectives/description

The flight system was mounted in a Cessna aircraft owned by Lincoln Laboratory equipped with a hole cut out of the bottom that allows for mounted scientific equipment to view the Earth below. The CRISP system was mounted such that its field of view was directly below the airplane (nadir). The Cessna flew at a speed of ~50 m/s, and at an altitude of 1675 m for all of our collected data.

3.1. Coastal: extended target spectra

Two flights were conducted in August 2018 along the coast of Massachusetts. The objective of these tests was to demonstrate the ability of the CRISP system to extract useful spectra from extended ground targets. A coastal environment was chosen for the ability to capture sand and ocean water in the same datasets. Ocean water appears largely as a blackbody radiator in the LWIR, whereas quartz-containing sand has several distinct LWIR features between 8 and 9 µm, making a coastal scene an ideal choice for evaluating a CRISP system.

Flights were conducted at two locations: the shoreline of Plum Island, MA on Aug. 20, 2018 from 12 to 4 pm (near 42°43′02.3″N 70°46′37.2″W); and Cape Cod, MA on Aug. 23, 2018 from 2 to 4 pm (near 41°51′31.9″N 69°57′04.5″W). The weather during both flights was sunny and warm with good visibility. Passes parallel to the shoreline were flown at an altitude of 1675 m, with a field-of-view (FOV) on the ground of 448 m × 336 m (15° × 11.25°), and a GSD of 0.7 m. With a flight speed of ~50 m/s and frame rate of 50 Hz, the image shifted ~1.39 GSD per frame.

Local reference measurements of the temperatures of the air, sand and ocean water were collected along the shorelines using a Type-K thermocouple (Cooper Atkins 50336-K coupled with a Fluke 80TK thermocouple module for digital multimeters). The air temperature was 21 °C at Plum Island (24 °C at Cape Cod), the water temperature was 22 °C at Plum Island (17–20 °C at Cape Cod), and the sand temperature was 29–44 °C at Plum Island (22–43 °C at Cape Cod), dependent on the location relative to the water. Local sand samples were also collected and used to provide spectral reflectance measured using an FTIR instrument in the laboratory. The atmospheric transmission from ground to 1675 m was modeled via MODTRAN (Berk et al., 2014) assuming a standard mid-latitude summer atmosphere with 74% relative humidity in the lower 1 km layer and 64% relative humidity in the 1–2 km layer. The relative humidity on the beach test flights was 70% (Plum Island) and 50–60% (Cape Cod). The MODTRAN model yielded an average transmission of 78% averaged over the 8–12 µm band. The transmission curve is relatively flat but dips on either end of the LWIR spectrum. It has a minimum of 53% near 8 µm, and a maximum of 87% near 9 µm. The weather during the coastal flights was mostly sunny (little cloud cover, with clouds never coming between the CRISP sensor and the ground during data collections).

3.2. Inland: Point targets and gas release

A flight was conducted in May 16, 2019 over Fort Devens, MA. The objectives of the tests were to (1) observe point targets to determine the PSF of the spectrometer during flight, as well as (2) demonstrate the ability to extract spectra from single pixel objects. Additionally, (3) a controlled gas release was performed in order to assess the ability of CRISP to identify gas releases. Similar to the previous flights, the plane

flew at an altitude of 1675 m with a velocity of ~50 m/s. The weather was mostly cloudy. The ground temperature was 20–25 °C.

Bright point targets were created using propane burners which heated charcoal filled cast iron skillets. These skillets were ~30 cm in diameter, encompassing ~1/5 of a GSD in area (for our 1675 m altitude flight). Three of the bright point targets were underneath thin films of different materials (the films were positioned ~2.5 m above the propane burners). Reference spectra of the three films had been measured with the CRISP spectrometer in the laboratory prior to the flight. The films were Kapton, Mylar, and Teflon, all 25.4 μm thick. An additional point target was left uncovered and served as a reference to aid in ascertaining the transmission spectrum of the three films.

The release of a known gas was timed to occur during the overflight. The gas was SF_6, which was released at a rate of 1.5×10^3 cm^3/s over ~30 s. It was released in the center of a 30 × 15 m sheet of aluminum foil, which was emplaced to reflect the cold sky background and thus ensure a temperature contrast between the airborne gas and the surface below it, without which no gas detection is possible (Manolakis et al., 2016).

Gas plume dynamics are driven by a combination of diffusion, drift and mixing with ambient air. In order to estimate concentration path-lengths, we assumed a simplified model in which wind in one direction plays a dominant role. Wind speeds were variable with estimated strengths of 2 m/s to 10 m/s, based on nearby weather station data. Assuming wind-driven drift dominates the gas dynamics, the gas extends in the wind direction to somewhere between 60 m (2 m/s wind) and 300 m (10 m/s wind). If we assume the gas diffuses 10 m in the other horizontal direction (consistent with our imagery) and a 1 m vertical expansion, the resultant gas volumes are $10 \times 60 \times 1$ m^3 and $10 \times 300 \times 1$ m^3. The corresponding concentration path-length of the gas plume ranges from 15 ppm-m to 75 ppm-m.

A schematic of the point target and aluminum foil setup is shown in Fig. 6a. The ground targets were setup near 42°30′20.5″N 71°39′53.6″W. The hot point targets and the aluminum foil sheet were placed in close proximity such that they could be imaged simultaneously from the CRISP system during a flyover. A CRISP image of the ground targets is shown in Fig. 6b (the image is cropped for better visibility of the targets). Photographs of the point targets and aluminum foil can be seen in Fig. 6c and d respectively.

4. Flight test results/analysis

Example imagery from the CRISP flight tests is shown in Fig. 7. Coastal imagery, urban imagery as well as sample imagery taken over our point target/gas release ground setup can be seen. In the coastal imagery (top set of images), we see a nice contrast in temperature between the relatively hot sand and the colder ocean water. Houses, streets and several industrial buildings are visible in the urban imagery (middle set of images). A large contrast in the apparent temperatures of the two separate industrial buildings is noted. The “colder” rooftop is likely made of a metal material which reflects the cold blue sky, making it appear as a lower temperature. In the third set of images (bottom), the 30 × 15 m sheet of reflective aluminum foil is clearly visible (as a dark, cold spot in the CRISP imagery), as well as the four bright point targets to the left of the aluminum foil. Six bright spots are visible in the third CRISP image in total, the two bright spots furthest to the left side are two cars parked in line with the bright point targets. The test targets were setup on a large patch of gravel surrounded by trees and/or dirt on all sides. The apparent fixed pattern noise in the raw, unprocessed CRISP imagery is caused by the encoding mask (residuals left behind from the recombination of the dispersed scene, encoded with a randomly-chosen binary grid). We note that these artifacts are not present in processed CRISP data.

A major benefit of our imaging spectrometer is the ability to

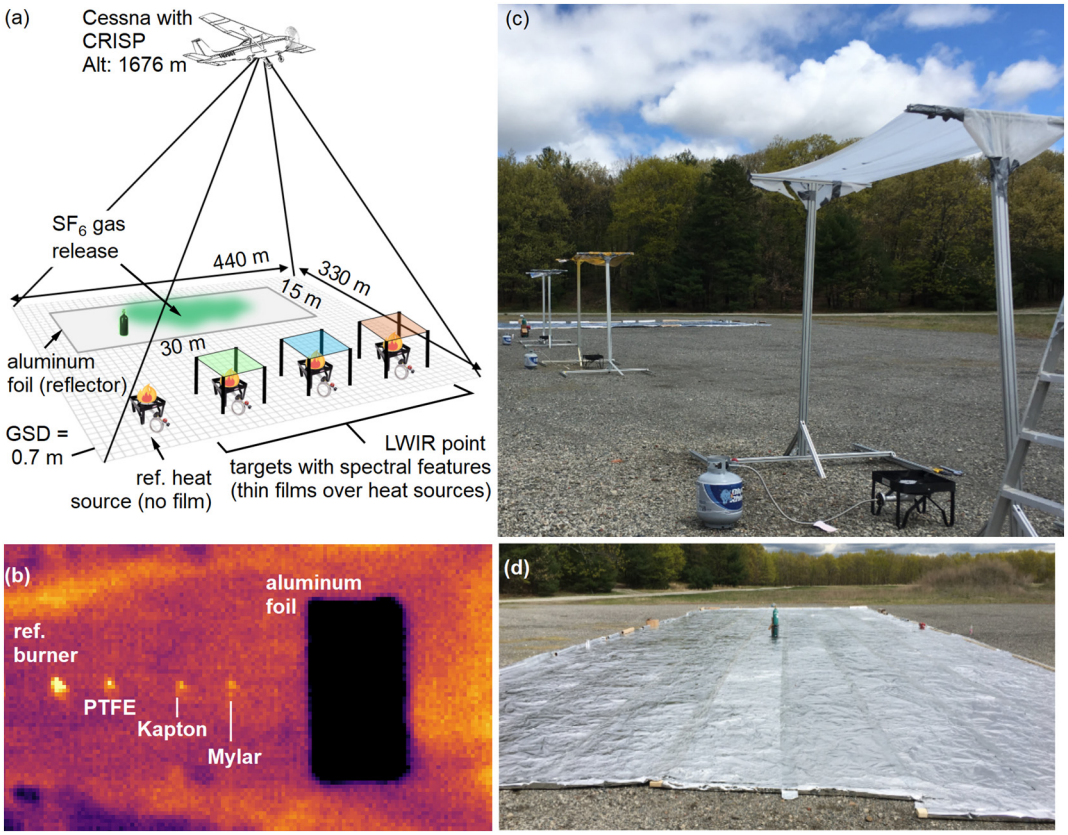

Fig. 6. Inland point target setup. (a) Schematic of flight targets; (b) CRISP LWIR image of the scene; (c) bright point sources (propane heated charcoal) covered by thin films; (d) Al foil with SF_6 cylinder used for gas release.

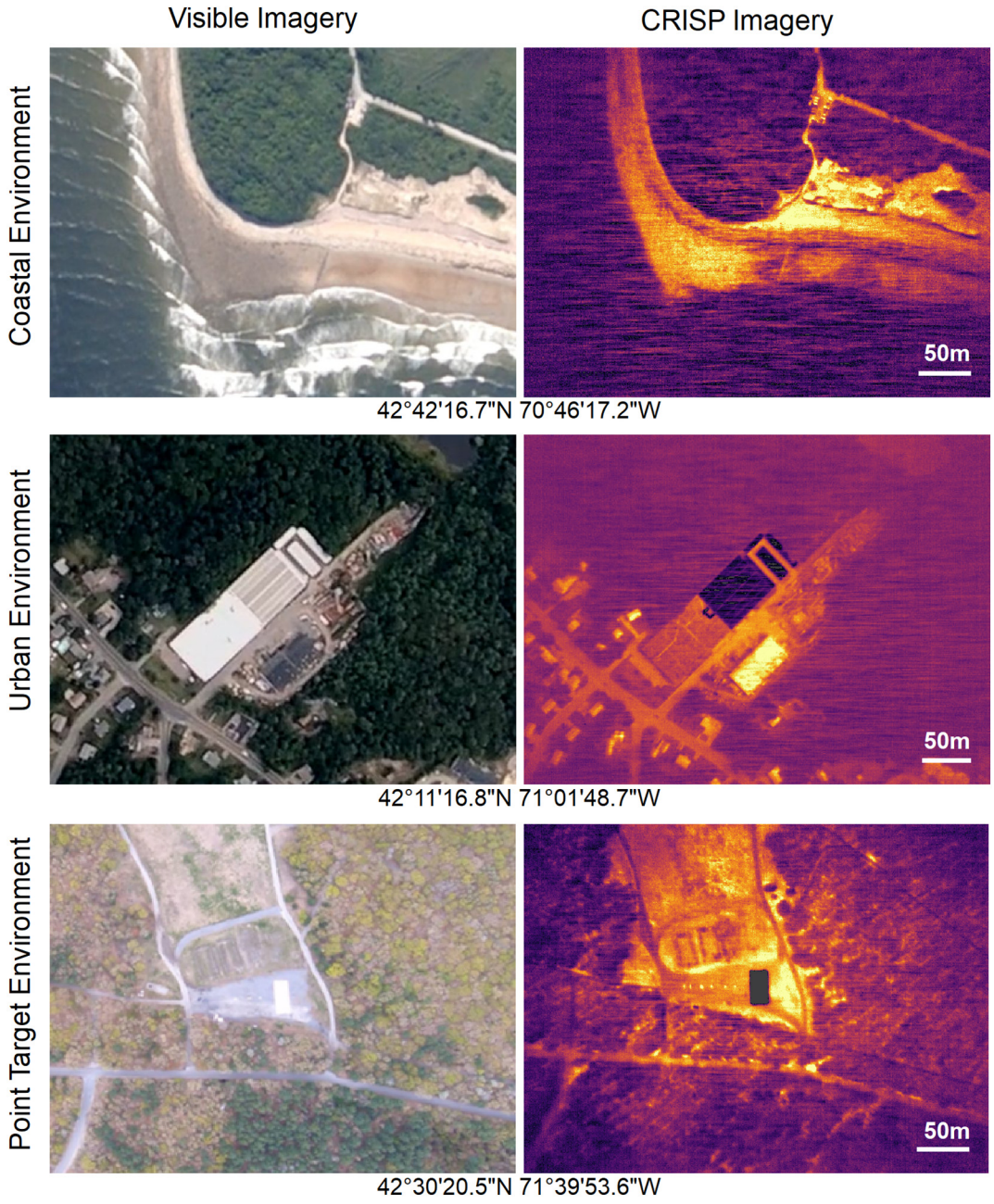

Fig. 7. Aerial images collected during the flight missions. Visible imagery (left), versus CRISP raw, i.e., unprocessed, imagery (right).

conduct frame-to-frame image registration for motion tracking. A simple frame-to-frame image registration algorithm was implemented to track targets in the CRISP datasets in order to process the data and create spectra. This algorithm is outlined in Fig. 8. A 2D cross correlation between every n-frames (for our data we used $n = 20$) in each dataset is computed and x- and y-translations are determined. We then interpolate these values to obtain translation data for each image in the dataset. In our tests, we determined that such an algorithm for motion tracking is adequate and comparable to tracking provided by our INS data. All spectra discussed in this work used CRISP-derived registration to remove motion artifacts and isolate targets.

4.1. Coastal

Emissivity spectra of sand and ocean water from coastal environments located in Plum Island, MA, and Cape Cod, MA are shown in Fig. 9. The spectra were produced by taking an average of a 15 px by 15 px area (~10.5 m × 10.5 m). Emissivities were calculated using the measured temperatures of the objects, and referencing the CRISP spectra to our calibrated blackbody data library collected in the lab prior to the flights. Note that atmospheric corrections were not included. Given that we estimated ~80% atmospheric transmission, we are neglecting the effects of 20% of the energy that manifests as upwelling and downwelling radiance. Since atmospheric transmission losses are greatest at the edges of the LWIR spectrum, exactly where our sensor sensitivity is most noisy, we found that corrections generally resulted in an even noisier spectrum. Nonetheless, the CRISP spectra of sand and water closely resemble sand and water spectra from the NASA Joint Emissivity Database Initiative (JEDI) (Hulley and Hook, 2009) and NASA ASTER databases (Baldridge et al., 2009; Meerdink et al., 2019a), respectively. Note that the CRISP data tends to overestimate the emissivity especially near emissivity minima. This difference between the apparent emissivity we report with CRISP and the literature results is exactly what one would expect given that we have not

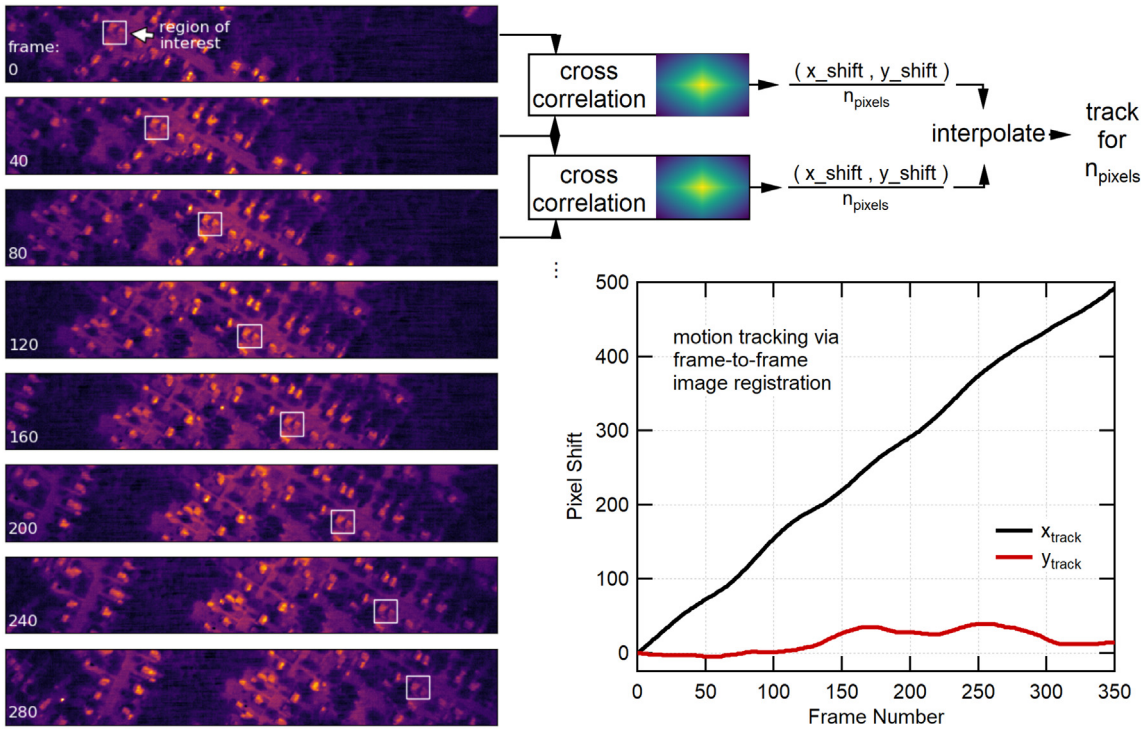

Fig. 8. Motion tracking using CRISP image data. Input imagery (right) and cross correlation output (right).

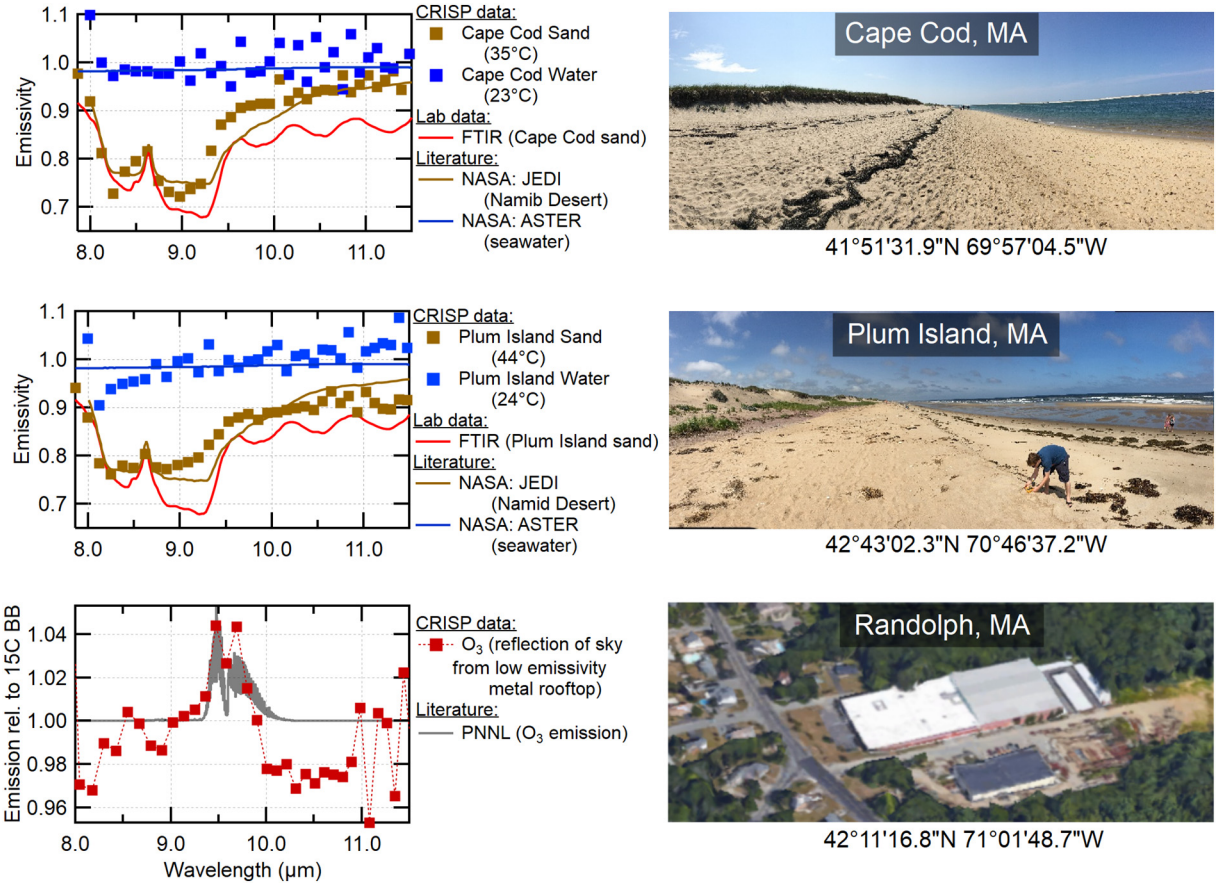

Fig. 9. Coastal CRISP spectra. Sand and ocean water spectra from (left, top) Cape Cod, MA, and (left, middle) Plum Island, MA. Atmospheric ozone emission was also captured with the CRISP system (left, bottom). Photographs of the locations of each dataset is shown in the right column.

accounted for the effects of downwelling radiance. Near the emissivity minima, more of the downwelling radiance is reflected from the sand, adding radiance at the detector and thus apparent emissivity. Additionally, we include a laboratory-collected D&P Instr. Model 102 FTIR spectrometer emissivity spectrum of a sand sample we collected from Plum Island. The FTIR spectrum of sand (the measurement was made by collecting the diffuse scatter off the sand and comparing that to the scattered light from an Infragold reference target) closely resembles our CRISP spectra, but includes a periodic oscillation between 9.5 and 11.5 μm. This oscillation is most likely caused by instrumental interferences (within the FTIR itself).

During the coastal flight campaign we collected CRISP data outside of our planned coastal area so that we could examine CRISP imagery of various types of terrain. This allowed for the possibility of capturing targets of opportunity. One such target of opportunity was a metal rooftop reflecting the cold blue sky above it [see Fig. 7 (middle)]. The LWIR temperature of the rooftop was estimated at 15 °C based on comparison to laboratory blackbody data. Emission of the metal rooftop relative to a 15 °C blackbody is pictured in Fig. 9 (bottom). Emission lines near 9.5 μm, which are greater than the background 15 °C blackbody radiation, reveal evidence of atmospheric ozone (O_3).

The expected ozone signal was estimated assuming a 25 °C uniform 80 ppb concentration (Di et al., 2017) of ozone throughout the entire column below the CRISP sensor. Given that the effective reflected roof temperature was 15 °C, we would not expect to observe significant emission from higher atmospheric O_3 as the temperature difference would vanish. Within the bounds of our air temperature measurements (21–25 °C), 25 °C yielded the best match to the expected maximum emission for an 80 ppb concentration of O_3. Thin plume and linear Planck function assumptions (Manolakis et al., 2016) yield the following relationship:

$$L = C_B \Delta T \tau_{atm} A \quad (1)$$

where L is the radiance change due to the plume, C_B is the change in blackbody radiance with temperature, ΔT is the temperature difference between plume and background, τ_{atm} is the atmospheric transmission, and A is the absorption due to the plume. Using this relationship, our estimated temperature difference (ΔT = 10 °C), estimated atmospheric transmission (τ_{atm} = 0.8), and an ozone spectrum from HITRAN (Rothman et al., 1987), the estimated emission from ozone matches the measured CRISP signal quite well (Fig. 9).

4.2. Point targets and gas release

An example overhead CRISP image of the point targets used to estimate PSF is shown in Fig. 7 (bottom). To calculate the PSF from the flight data, we fit Gaussians to the reference propane burner (the propane burner without a film elevated above it) for various locations across the focal plane (unprocessed, raw data) and took an average of the Gaussian fits. The average Gaussian fit is shown in Fig. 10 (left, top), and has a FWHM of $PSF_{unprocessed}$ = 2.8 px. We also measured the PSF of CRISP processed data by fitting a Gaussian to a point target in a CRISP processed hyperspectral cube. The PSF after CRISP processing is negligibly different from the unprocessed data, with a FWHM of $PSF_{processed}$ = 2.9 px, (Fig. 10 left, bottom).

The theoretical (Airy disc) diffraction-limited PSF for the CRISP spectrometer is $FWHM_{PSF}$/px = 1.07, for a 17 μm pixel. This value is a weighted mean for the λ = 7.7–14 μm wavelength span of the spectrometer. The measured flight PSF of the CRISP system is larger than the theoretical motionless value for two reasons: (1) the velocity of the aircraft during data collections was slightly faster than the ideal velocity of 1 GSD/frame, resulting in some blurring of the PSF; and (2), the frame-to-frame pitch/roll jitter caused by vibrations in the aircraft. Aircraft velocity during CRISP data collects was ~50 m/s, which equates to 1.39 GSD/frame. INS data yield typical frame-to-frame jitter values of 0.152 px (pitch) and 0.675 px (roll) [see Fig. 10 (right) for typical data]. We account for these two phenomenon via the simple relationship:

$$PSF_{flight} = (PSF_{CRISP,Motionless} – jitter) \bullet velocity \quad (2)$$

This yields $PSF_{CRISP,\ Motionless}$ = 1.10 px, which is within 2.76% of the theoretical diffraction-limited spot size noted above.

Transmission spectra of our three thin-film point targets (Kapton, Mylar and Teflon) captured with the CRISP system during flight are shown in Fig. 11. Spectra of the thin films processed from a single dataset (one flight over the point targets, ~316 frames captured) are shown in the right column. Average spectra from all flyovers (9 total flights) are shown in the left column. Reference spectra (collected with the CRISP system of the same films in the laboratory) are shown in the plots as a black dotted line. In each spectrum, the raw data are represented as small dots. The larger markers represent the spectra after processing with a locally-weighted regressing smoothing algorithm (LOESS). The transmission spectra collected during flight closely resemble the reference data collected in the laboratory, demonstrating that CRISP is able to extract useful spectra from point targets.

Results from a release of SF_6 gas during a flyover are shown in Fig. 12. At λ_1 = 10.55 μm, a strong feature exists in the SF_6 LWIR spectrum (Sharpe et al., 2004), which can be seen in Fig. 12b. Fig. 12a shows a heatmap of the location of the SF_6 gas during the release over the aluminum foil. A heatmap of a nonrelease is also shown for reference. To produce these heatmaps, we plot the ratio of two wavelengths, λ_1/λ_2, where λ_1 is on resonance and λ_2 is off resonance (10.36 μm). 4 × 4 pixel spectral binning was used to achieve a higher signal-to-noise (SNR) ratio for better clarity. The SF_6 is clearly evident in the center of the aluminum foil, especially when compared to a dataset with no gas release.

We compare CRISP's observed absorption change of ~100% (signal

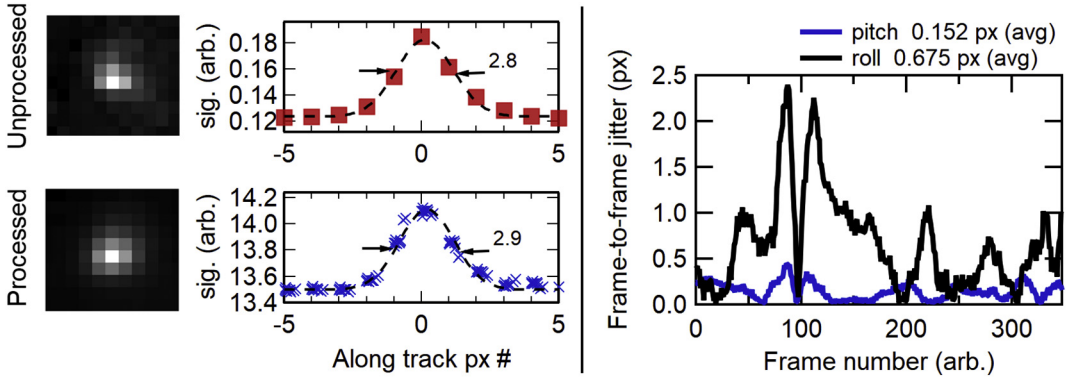

Fig. 10. CRISP point spread function: image (left) and along-track cross section (middle). Raw unprocessed data and post CRISP processed data are both shown. (Right) typical frame-to-frame aircraft pointing jitter (pitch, roll, in units of pixels) during the flight.

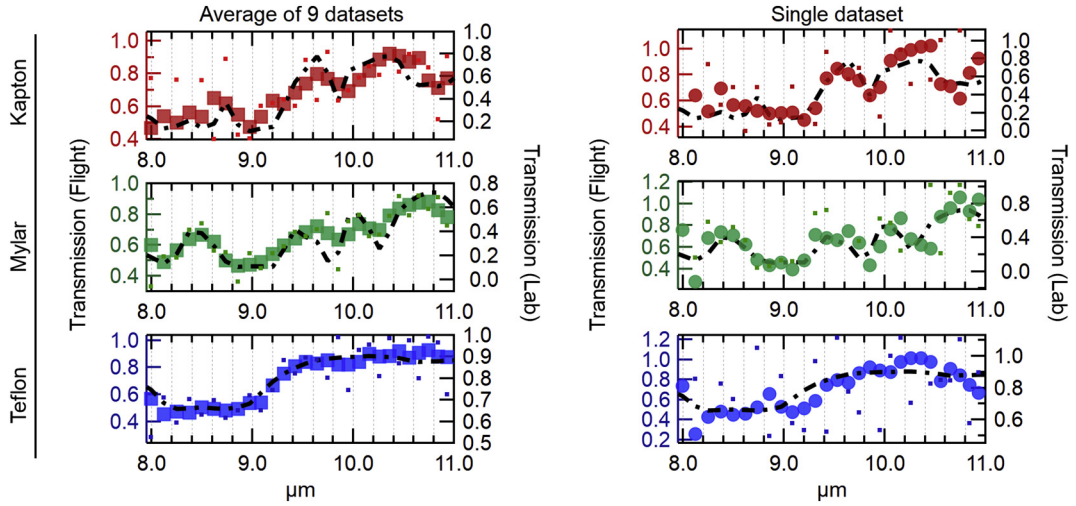

Fig. 11. Transmission spectra of thin films positioned over bright point sources. Transmission is calculated relative to an unobstructed (no films) bright point source. In each spectrum, black dashed lines are CRISP data measured in the laboratory. Raw data is represented as small dots, and the larger markers represent the spectra after processing with a locally-weighted regressing smoothing algorithm (LOESS). The left-hand side is an average over 9 overflights, while the right-hand side is from a single flight.

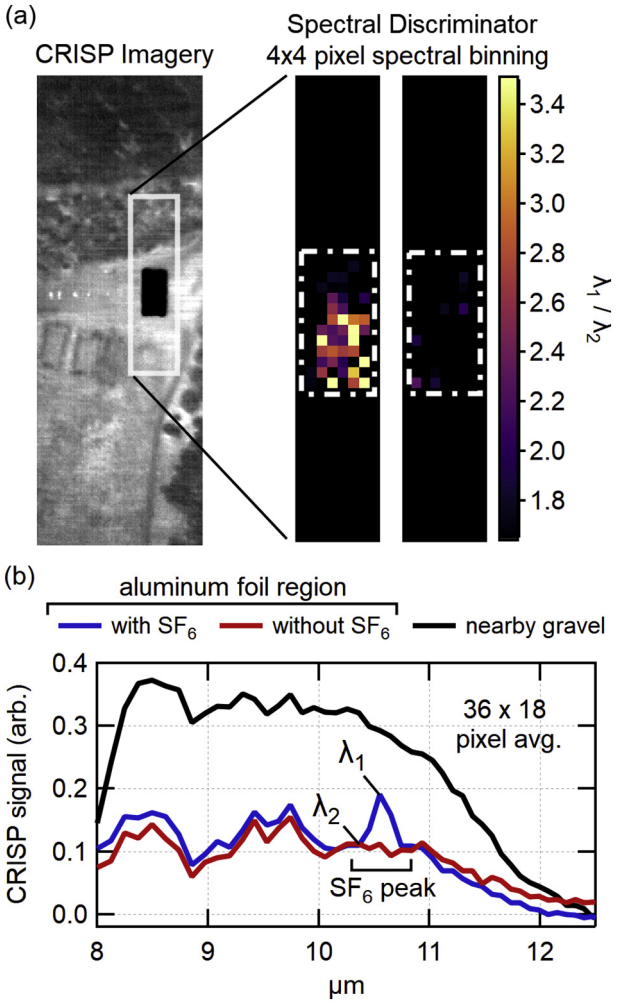

Fig. 12. SF_6 gas release detection. (a) Broadband LWIR imagery (top left) next to imagery of a spectral discriminant (top right) designed to detect SF_6 (see text). The middle panel is the discriminant in the presence of the gas release, while the right panel is the discriminant in the absence of a release; (b) CRISP spectra of the aluminum foil both with and without the gas release, and nearby gravel.

with SF_6 relative to signal without SF_6) to gas concentration levels as follows. We once again assume a thin plume and linear Planck function (Manolakis et al., 2016), and make use of Eq. (1). An estimate of the temperature difference, ΔT, between the gas plume and ground below is necessary in order to calculate the plume's concentration path-length. We measured the gas temperature at the nozzle (13 °C) and directly in front of the nozzle at a range of ~0.6 m (18 °C). The air temperature was 25 °C. We estimate the background aluminum foil temperature (reflecting the cold sky) at −12 °C based on a comparison of its spectrum to an extrapolation of our radiative calibration data, though we note that this is an extrapolation beyond our calibration range with associated error of ± 12 °C. We thus bound ΔT at an upper limit of 37 °C and a lower limit of 13 °C. Using our MODTRAN estimate of $\tau = 0.8$ and the PNNL absorption for SF_6 of 0.047 $ppm^{-1}\ m^{-1}$ at 10.55 μm (Sharpe et al., 2004), we estimate the concentration-pathlength between 9 and 25 ppm-m. Our estimates based on actual gas flow rates (vide supra) put the gas concentration-pathlength between 15 and 75 ppm-m, in reasonable agreement with these estimates based on the CRISP spectra.

4.3. Comparison to other systems

Numerous HSI systems operating in the LWIR have been conceived over the years. Table 1 compares CRISP to some of the more successful and more recent systems. While it does not have the sensitivity (NESR) of the cooled systems, it is competitive (53 μflicks) with the uncooled system (TIRCIS), and maintains a size, weight and power advantage over the cooled systems. In a previous paper (Sullenberger et al., 2017), we estimated that the system was achieving ~1/2 its theoretical performance gains. The deviation from the theoretical limit was likely due to issues with optical aberrations and how they were addressed algorithmically.

We expect that CRISP's overall performance could be improved in several ways: reducing optical aberrations along with algorithmic improvement (~2× improvement), increasing optical throughput via better optical elements (~2× improvement), and utilization of a lower noise focal plane (~2× improvement). We measured an average NETD of 95 mK for the current CRISP system by staring at a room temperature calibrated blackbody and recording the standard deviation of each pixel over time (note that both the spatial and temporal values were the same, and also that this value did not change when staring at liquid nitrogen, indicating we are indeed sensor noise limited). This number

Table 1
Comparison of CRISP to other state-of-the art LWIR HSI systems. NESR (noise equivalent spectral radiance) and NETD (noise equivalent temperature difference) relate to system sensitivity. BIB = blocked impurity band; SLS = strained layer superlattice; MCT = mercury cadmium telluride; FP = Fabry Perot.

	CRISP	SEBASS	MAKO	HyperCam (TELOPS)	Sagnac	TIRCIS	HyTi	HyTes
Operational status	Airborne flight	Airborne flight	Airborne flight	Airborne flight	Airborne flight	Satellite launch failure	Ground Testing	Airborne flight
Spectrometer type	Coded dual disperser	Pushbroom	Whisk-broom	FTIR	Sagnac interfere-ometer	Variable gap FP interferometer	Variable gap FP interferometer	Pushbroom
Detector	Uncooled μbolometer	Cooled BIB	Cooled BIB	Cooled MCT	Cooled MCT	Uncooled μbolometer	Cooled SLS	Cooled QWIP (Quantum-well IR photodector)
Spectral range (resolution)	8–12 μm (94 nm)	7.6–13.5 μm (50 nm)	7.6–13.2 μm(44 nm)	7.8–11.8 μm(40 nm)	7.5–11 μm(200 nm)	8–14 μm(87 nm)	8–10.7 μm(130 nm)	7.5–12 μm(18 nm)
Frame rate	50 Hz	244 Hz	3255/4 Hz		233 Hz	60 Hz	160 Hz	35/22 Hz
NESR	**Current:** 53 μflicks, NETD 3.5 K **Projected:** 2.7 μflicks, NETD 0.18 K	0.8 μflicks	0.6 μflicks		2 μflicks	NETD < 1 K	NETD ~ 0.1 K	NETD 0.2 K
Ref.	This work	Hackwell and et al., 1996	Hall et al., 2016	Agassi et al., 2016	Lucey et al., 2012	Wright et al., 2016	Wright, 2019	Hulley et al., 2016

(i.e., NETD of 95 mK) represents the detector noise per pixel not the spectrally-binned spectrometer noise per wavelength. Overall performance could be additionally improved by using a larger format imager (1920 × 1200 pixels uncooled arrays are now available, yielding ~6× more frames for integration). The NESR is expected to scale linearly with optical throughput and focal plane noise. We have shown (Sullenberger et al., 2017) that the NESR scales as the square root of the number of frames for integration. Thus we estimate that an ultimate system could be improved by a factor of 2·2·2·2.5 = 20×, where we have assumed that elimination of aberrations and algorithmic improvement will achieve the theoretical performance gains predicted by theory. The NESR of such a system would be 2.7 μflicks.

An uncooled LWIR HSI system with this sensitivity offers intriguing potential possibilities. Weather sensing, in particular atmospheric sounding, relies on hyperspectral imagery to generate data products such as atmospheric water vapor and temperature profiles. Small space platforms have become a very significant focus in the commercial industry. Leveraging these small form factors is of great interest for future weather sensing systems. CRISP could play a significant role in this transition. The spectral sensitivity of NOAA's GOES-R weather sounding satellite is 1.5 μflick in the LWIR (Schmit et al., 2012). The LWIR sensitivity of the Cross-Track Infrared Sounder (CrIS) Fourier Transform Michelson interferometer instrument launched on board the Suomi National Polar-Orbiting Partnership as part of a series of next-generation U.S. weather satellites is 1.4 μflick (Han et al., 2013). As mentioned above, the projected sensitivity of CRISP is 2.7 μflick. However, both these other systems require cryogenic cooling, in contrast to CRISP. CRISP's form factor is significantly smaller, opening up the possibility of launching multiple CRISP sensors on a collection of small satellites. The resultant sounding array could offer advantages over current systems, including the advantages of viewing a scene from multiple look angles simultaneously and/or improved coverage and revisit rates.

5. Conclusions

In summary, we have successfully demonstrated the ability to collect airborne LWIR spectra from an imaging spectrometer that uses an uncooled microbolometer detector array. We captured hard target (sand and ocean water) emissivity spectra from coastal regions at an altitude of 1675 m. Additionally, we captured transmission spectra of three different point targets from a similar altitude. Finally, we detected gas species including a release of SF_6 gas and were able to produce a heatmap showing the location of the gas.

Authors' contribution

C. M. Wynn: Conceptualization, Methodology, Validation, Formal Analysis, Investigation, Data Curation, Writing- Original Draft, Writing-Review & Editing, Supervision, Project administration, Funding acquisition, **J. Lessard**: Investigation, Resources, Methodology, **A. B. Milstein**: Conceptualization, Funding acquisition, **P. Chapnik**: Resources, **Y. Rachlin**: Conceptualization, Methodology, Funding acquisition, **C. Smeaton**: Resources, **S. Leman**: Resources, **S. Kaushik**: Supervision, Project administration, Funding acquisition, and **R. M. Sullenberger:** Conceptualization, Methodology, Validation, Formal Analysis, Investigation, Data Curation, Writing- Original Draft, Writing-Review & Editing, Visualization, Supervision, Project administration, Software.

Funding

Distribution Statement A. Approved for public release. Distribution is unlimited. This material is based upon work supported by the Under Secretary of Defense for Research and Engineering under Air Force Contract No. FA8702-15-D-0001. Any opinions, findings, conclusions or recommendations expressed in this material are those of the author(s) and do not necessarily reflect the views of the Under Secretary of Defense for Research and Engineering.

Declaration of competing interest

The authors declare that they have no known competing financial interests or personal relationships that could have appeared to influence the work reported in this paper.

Acknowledgments

We gratefully acknowledge the feedback and guidance from our fellow colleague Ronald Lockwood.

References

Agassi, E., Hirsch, M., Chamberland, M., Gagnon, and Eichstaedt, H., "Detection of gaseous plumes in airborne hyperspectral imagery," Proc. SPIE **9824**, Chemical, Biological, Radiological, Nuclear, and Explosives (CBRNE) Sensing XVII, 98240U

(2016).
Baldridge, A.M., Hook, S.J., Grove, C.I., Rivera, G., 2009. The ASTER spectral library version 2.0. Remote Sens. Environ. 113, 711.
Berk, A., Conforti, P., Kennett, R., Perkins, T., Hawes, F., van den Bosch, J., 2014. Modtran® 6: A Major Upgrade of the Modtran® Radiative Transfer Code. pp. 1–4.
Calderón, R., Navas-Cortés, J.A., Lucena, C., Zarco-Tejada, P.J., 2013. High-resolution airborne hyperspectral and thermal imagery for early detection of Verticillium wilt of olive using fluorescence, temperature and narrow-band spectral indices. Remote Sens. Environ. 139, 231.
Di, Q., Rowland, S., Koutrakis, P., Schwartz, J., 2017. A hybrid model for spatially and temporally resolved ozone exposures in the continental United States. J. Air Waste Manage. Assoc. 67, 39.
Hackwell, J.A., et al., 1996. LWIR/MWIR imaging hyperspectral sensor for airborne and ground-based remote sensing. In: Proc. SPIE. 2819. pp. 102.
Hagen, N., Kudenov, M.W., 2013. Review of snapshot imaging technologies. Opt. Eng. 52, 90901.
Hall, J.L., Boucher, R.H., Buckland, K.N., Gutierrez, D.J., Keim, E.R., Tratt, D.M., Warrant, D.W., 2016. Mako airborne thermal infrared imaging spectrometer- performance update. In: Proc. SPIE. 9976 99764-1.
Han, Y., et al., 2013. Suomi NPP CrIS measurements, sensor data record algorithm, calibration and validation activities, and record data quality. J. Geophys. Res. Atmos. 118 (12734).
Honniball, C.I., Wright, R., Lucey, P.G., Crites, S.T., 2016. The miniaturized infrared detector of atmospheric species (MIDAS) a low-mass, MWIR low-power hyperspectral imager. Proc. SPIE 9819 98190J-1.
Hulley, G.C., Hook, S.J., 2009. The north American ASTER land surface emissivity database (NAALSED) version 2.0. Remote Sens. Environ. 113, 1967. https://emissivity.jpl.nasa.gov/.
Hulley, G.C., Duren, R.M., Hopkins, F.M., Hook, S.J., Vance, N., Guillevic, P., Johnson, W.R., Eng, B.T., Mihaly, J.M., Jovanovic, V.M., Chazanoff, S.L., Staniszewski, Z.K., Kuai, L., Worden, J., Frankenberg, C., Rivera, G., Aubrey, A.D., Miller, C.E., Malakar, N.K., Sánchez Tomás, J.M., Holmes, K.T., 2016. High spatial resolution imaging of methane and other trace gases with the airborne hyperspectral thermal emission spectrometer (HyTES). Atmos. Meas. Tech. 9, 2393.
Leifer, I., Melton, C., Tratt, D.M., Buckland, K.N., Clarisse, L., Coheur, P., Frash, J., Gupta, M., Johnson, P.D., Leen, J.B., Van Damme, M., Whitburn, S., Yurganov, L., 2017. Remote sensing and in situ measurements of methane and ammonia emissions from a megacity dairy complex: chino, CA. Remote Sens. Environ. 221, 37.
Lucey, P.G., et al., 1998. AHI: An airborne long wave infrared hyperspectral imager. In: Proc. SPIE. 3431. pp. 36.
Lucey, P.G., Horton, K.A., Williams, T., 2008. Performance of a long-wave infrared hyperspectral imager using a Sagnac interferometer and an uncooled microbolometer array. Appl. Opt. 47, F107.
Lucey, P.G., Wood, M., Crites, S.T., Akagi, J., 2012. A LWIR hyperspectral imager using a Sagnac interferometer and cooled HgCdTe detector array. Proc. SPIE 8390, 83900Q-1.
Manolakis, D., Lockwood, R., Cooley, T., 2016. Hyperspectral Imaging Remote Sensing. Cambridge Univ. Press, Cambridge, UK.
Manolakis, D., Pieper, M., Truslow, E., Lockwood, R., Weisner, A., Jacobson, J., Cooley, T., 2019. Longwave infrared hyperspectral imaging. IEEE Geo. Rem. Sens. Mag 7, 72.
Meerdink, S.K., Hook, S.J., Roberts, D.A., Abbott, E.A., 2019a. The ECOSTRESS spectral library version 1.0. Remote Sens. Environ. 230, 111196.
Meerdink, S.K., Roberts, D.A., Hulley, G., Gadera, P., Pisekd, J., Adamsond, K., King, J., Hook, S.J., 2019b. Plant species' spectral emissivity and temperature using the hyperspectral thermal emission spectrometer (HyTES) sensor. Remote Sens. Environ. 224, 421.
Mouroulis, P., Green, R.O., Chrien, T.G., 2000. Design of pushbroom imaging spectrometers for optimum recovery of spectroscopic and spatial information. Appl. Opt. 39, 2210.
Myhre, G., Shindell, D., Breon, F.-M., Collins, W., Fuglestvedt, J., Huang, J., Koch, D., Lamarque, J.-F., Lee, D., Mendoza, B., Nakajima, T., Robock, A., Stephens, G., Takemura, T., Zhang, H., 2013. Anthropogenic and natural radiative forcing. In: Stocker, T.F., Qin, D., Plattner, G.-K., Tignor, M., Allen, S.K., Boschung, J., Nauels, A., Xia, Y., Bex, V., Midgley, P.M. (Eds.), Climate Change 2013: The Physical Science Basis. Contribution of Working Group I to the Fifth Assessment Report of the Intergovernmental Panel on Climate Change. Cambridge University Press, Cambridge, United Kingdom, pp. 659–740.
Rothman, L.S., Gamache, R.R., Goldman, A., Brown, L.R., Toth, R.A., Pickett, H.M., Poynter, R.L., Flaud, J.-M., Camy-Peyret, C., Barbe, A., Husson, N., Rinsland, C.P., Smith, M.A.H., 1987. The HITRAN database: 1986 edition. Appl. Opt. 26, 4058.
Schmit, T., Gunshor, M., Fu, G., Rink, T., Bah, K., 2012. GOES-R Advanced Baseline Imager (ABI) Algorithm Theoretical Basis Document for Cloud and Moisture Imagery Product (CMIP), Version 3.0.
Sharpe, S.W., Johnson, T.J., Sams, R.L., Chu, P.M., Rhoderick, G.C., Johnson, P.A., 2004. Gas-phase databases fro quantitative infrared spectroscopy. Appl. Spectrosc. 58, 1452.
Sullenberger, R.M., Milstein, A.B., Rachlin, Y., Kaushik, S., Wynn, C.M., 2017. Computational reconfigurable imaging spectrometer. Opt. Express 25, 31960.
Wright, R., 2019. "HyTi Hyperspectral Thermal Imager," Presented at NASA ESTO Forum. https://esto.nasa.gov/forum/estf2019/presentations/wright_S9P1_estf2019.pdf.
Wright, R., Lucey, P., Crites, S., Garbeil, H.M., Wood, E., Pilger, Gabrieli, A., Honniball, C., 2016. TIRCIS: thermal infrared compact imaging spectrometer for small satellite applications. Proc. SPIE 9880, 98801K-1.
Zarco-Tejada, P.J., González-Dugo, V., Berni, J.A.J., 2012. Fluorescence, temperature and narrow-band indices acquired from a UAV platform for water stress detection using a micro-hyperspectral imager and a thermal camera. Remote Sens. Environ. 117, 322.